Acta Geotechnica (2025) 20:4631–4650
https://doi.org/10.1007/s11440-025-02640-9

RESEARCH PAPER

Novel observations for the impact of particle morphology on shear modulus of granular materials

Shao-Heng He[1,2] · Zhen-Yu Yin[1,2] · Zhi Ding[3] · Rui-Dong Li[1,2]

Received: 18 November 2024 / Accepted: 21 April 2025 / Published online: 2 June 2025

Abstract

The influence of particle shape on the shear modulus at very small strain (G_{max}) of granular materials remains poorly understood and correlated. Using both micro-CT and bender element tests, this study aims to further systematically investigate this influence by comparing six granular materials with distinct particle shapes. The study included materials with angular and rounded particles, as well as relatively spherical and moderately angular particles, with particle morphological factors assessed using micro-CT. A series of bender element tests was conducted on these materials under various relative densities (D_r) and mean effective stresses (p'). Additionally, computed tomography (CT) technique was employed to interpret the role of particle shape on G_{max} from a microstructural perspective. The test results reveal that under the same relative density condition, as the irregularity of particle shape increases, the G_{max} of the materials first increases and then decreases. Angular materials exhibit the lowest G_{max} values, primarily due to their larger void ratio, while the mediumly angular materials display the highest G_{max} values compared to rounded and angular materials. Additionally, it was observed that overall regularity (OR) can be used to describe the significant transitional G_{max} response of granular material in relation to the variations in particle morphology. As OR decreases, the sensitivity of G_{max} to p' initially decreases and then increases, which was found to be related to the shape-dependent particle mean coordination number ($\overline{Z}$). Notably, in materials with an extremely low $\overline{Z}$ value, G_{max} exhibits a significantly faster increase with p'. Consequently, based on test data from granular materials with a wide range of particle shapes and transitional G_{max} responses, practical equations for correlating the parameters of G_{max} prediction model with particle morphology were formulated and validated.

Keywords Dynamic properties · Granular materials · Laboratory tests · Small-strain modulus

✉ Zhen-Yu Yin
zhenyu.yin@polyu.edu.hk

Shao-Heng He
heshaoheng@zju.edu.cn

Zhi Ding
dingz@zucc.edu.cn

Rui-Dong Li
22072096r@connect.polyu.hk

[1] Department of Civil and Environmental Engineering, The Hong Kong Polytechnic University, Hung Hom, Kowloon 999077, Hong Kong, China

[2] The Guangdong-Hong Kong Joint Laboratory for Marine Infrastructure, The Hong Kong Polytechnic University, Hung Hom, Kowloon 999077, Hong Kong, China

[3] Department of Civil Engineering, Hangzhou City University, Hang Zhou 310015, China

1 Introduction

Understanding the small-strain shear modulus (G_{max}) is crucial for accurately predicting the behavior of granular materials under different dynamic and static loading scenarios, enabling engineers and researchers to make informed decisions regarding project design [6, 18, 33, 34, 39, 47, 48, 53]. Besides the resonant column (RC) method, the bender element (BE) method has been employed to determine G_{max} by measuring the velocity of the shear wave propagating through the specimen [10, 13]. The difference in G_{max} measurements between BE and RC is generally less than 10% [7, 14, 56, 57]. Numerous experimental studies based on BE tests have been conducted to investigate the impact of mean effective stress (p'), void ratio (e), and particle size distribution on G_{max} of

granular materials [11, 25, 37, 56]. Among these factors, p' and e were found to play the most crucial role in determining G_{max}, while particle size distribution has a secondary role. Hardin and Richart [19] proposed a predictive model for G_{max} incorporating p' and e, which has been widely utilized in geotechnical engineering. Subsequently, the relationship between G_{max} prediction model parameters and grading factors was established [35, 38, 54]. More recent studies have emphasized the importance of establishing G_{max} model parameters and their relationship with various particle characteristics in practical engineering applications [12, 23, 36, 37, 40, 43].

Although there have been extensive investigations on the G_{max} behavior of granular materials, the current understanding regarding the influence of particle shape on G_{max} values is still limited and subject to debate. Hardin [15] found that Ottawa sand, which has a relatively rounded shape, has a higher G_{max} value compared to angular quartz sand with the same relative density, primarily due to the smaller void ratio of the former. They concluded that variations in G_{max} caused by different particle shapes can be attributed to variances in void ratio. Similarly, studies by Hardin and Richart [19] and Hardin and Drnevich [17] have demonstrated that particle shape has a negligible impact on G_{max} for granular soils, and the variations in G_{max} among different materials are primarily attributed to the shape-induced changes in void ratio. However, Bui et al. [6] summarized the relationship between void ratios and normalized G_{max} of various geo-materials. They argued that when the void ratios of different soils overlap, normalized G_{max} exhibits significant variations within a large range, indicating that G_{max} is influenced by particle characteristics such as particle size distribution and shape. Giang, et al. [11] conducted BE tests on calcareous sand and silica sand, and their findings revealed that G_{max} increases as the particle shape becomes more angular and less spherical due to the better fabric of angular materials for shear wave propagation. However, based on the database of shear wave velocity measured by BE tests, Cho et al. [8] reported that increasing particle irregularity leads to a decrease in G_{max}. Additionally, G_{max} of angular materials was found to exhibit heightened sensitivity to confining pressure compared to rounded materials. Payan [44] established a correlation between the small-strain stiffness of granular materials and particle shape parameters, noting that particles with higher regularity exhibit higher G_{max} values. Furthermore, Asadi et al. [5] conducted BE tests on natural pumiceous (NP) sand and Toyoura sand. Their results showed that NP sand, characterized by a more angular and elongated shape, possesses a smaller G_{max} compared to Toyoura sand. Besides, NP sand also displayed greater sensitivity to confining pressure in terms of its G_{max} values. More recently, Sarkar et al. [49] performed RC tests on crushed glass, natural sand, and glass beads, finding similar results that G_{max} increases with the increase in roundness and sphericity. Additionally, they observed that particle shape affects the G_{max} model parameters and subsequently established correlations between G_{max} model parameters and particle morphological factors. Currently, there is still some uncertainty regarding whether the G_{max} values of angular or rounded materials are greater, and whether the parameters of the G_{max} model are influenced by particle morphology. Consequently, this uncertainty can create difficulties when making accurate judgments about design and safety evaluations in practical projects. Moreover, previous experimental studies have primarily focused on a limited number of granular materials (typically around two or three types) and a small number of shape indicators to establish the correlation between particle shape and G_{max} prediction model. However, in practical engineering applications, the shapes of sand particles vary significantly, rendering the existing correlations for the parameters of G_{max} model, which are based on a limited range of granular materials, inadequate for all scenarios. Hence, further investigation is warranted to comprehend the impact of particle shape on G_{max} behavior.

To address the aforementioned issues, six granular materials with a uniform size but distinct particle shapes were employed for comparison. Particle shape analysis was performed on these materials to determine their morphological characteristics. The internal structure differences induced by particle shape were visually revealed using computer tomography (CT) scanning. Furthermore, bender element tests were conducted under triaxial conditions on these granular materials at various mean effective stresses and relative densities. A systematic analysis was conducted to reveal the influence of particle shape on the value of G_{max} as well as the sensitivity of G_{max} to p' and e. Additionally, this study elucidated the impact of particle shape factors on the prediction model for G_{max}. Moreover, practical equations for correlating the parameters of the G_{max} model in granular materials with particle morphology were formulated and validated.

2 Test materials and method

2.1 Test materials

As illustrated in Fig. 1a–f, four types of artificial glass beads—round, frosted, concave, and convex—were utilized alongside completely decomposed granite (CDG) sand from Hong Kong and Fujian sand (recognized as standard sand in China) as test materials to investigate the influence of particle shape on the behavior of G_{max}. To

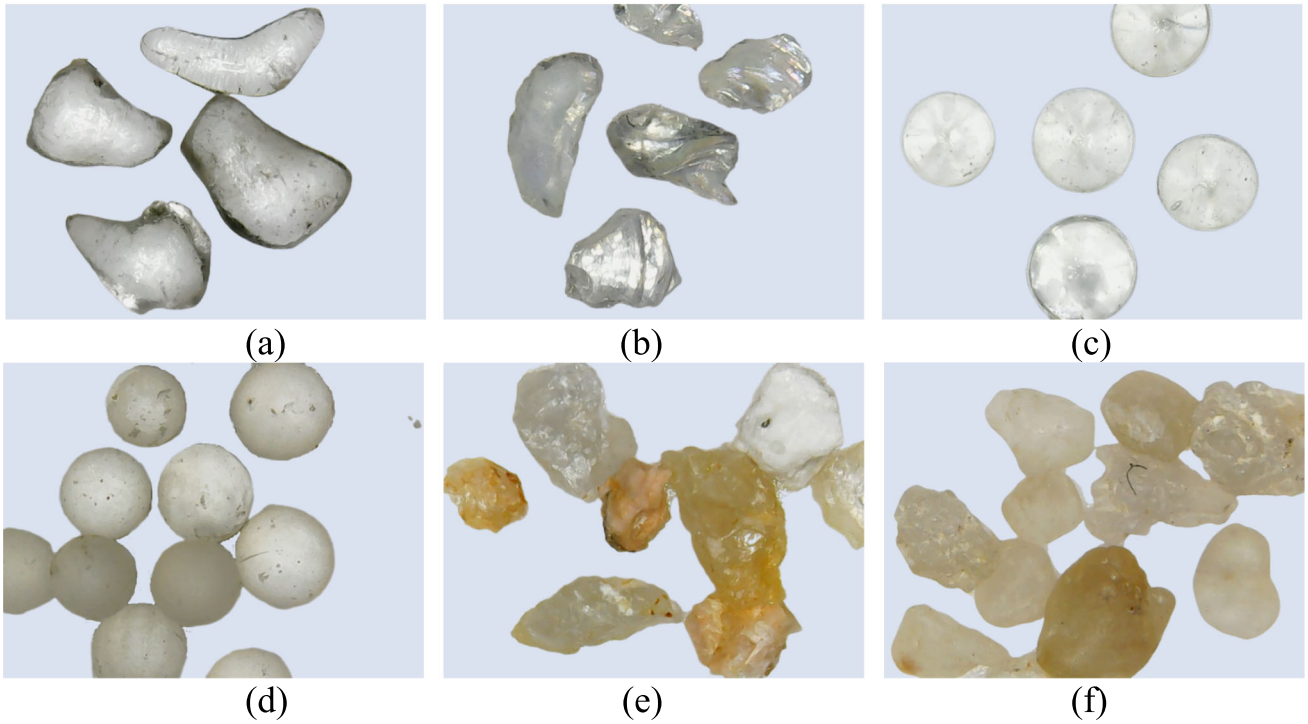

Fig. 1 Test materials: **a** Concave glass beads; **b** Convex glass beads; **c** Round glass beads; **d** Frosted glass beads; **e** CDG sand; **f** Fujian sand

mitigate the influence of the mean particle size (d_{50}) and isolate the impact of particle shape, this study utilized 1 mm and 2 mm sieves to screen natural sand and commercially produced artificial glass beads. Consequently, six granular materials with comparable particle sizes within the range of 1–2 mm were prepared. Frosted glass beads are produced by scratching the surface of round glass beads, resulting in a rougher surface texture. All materials were carefully arranged in a flat position and underwent computer tomography (CT) scanning [24]. This scanning process resulted in two-dimensional micro-images that clearly displayed the contours of the particles. To ensure the accuracy of the analysis, hundreds of individual particles were meticulously examined, and their morphological factors were calculated for each material. The evaluation encompassed determining four frequently employed particle shape indices, namely sphericity (S), aspect ratio (AR), convexity (C), and roundness (R), for each tested material. These indices provide a comprehensive understanding of the morphological properties of the particles [20, 31, 45, 46]. Here, S represents the ratio of the perimeter of a circle with the same area as the projected area of the grain to its actual perimeter; AR is the ratio between the minimum diameter (D_{min}) and the maximum diameter (D_{max}); C is calculated by dividing the grain's area (S_A) by the area that would result if any concavities within its perimeter were filled (i.e., $S_A + S_B$); R is determined as the ratio of the average of the radii of surface feature curvature (r_{ave}) to the radius of the maximum inscribed sphere (r_{max}), as illustrated in Fig. 2. The overall regularity OR is the average of the four shape indicators mentioned above.

The surface roughness of six granular materials was assessed using a CounourGT-K optical interferometer manufactured by Bruker Instruments Ltd, Germany [20]. The average roughness (R_a) was employed as a quantifiable measure [2]. R_a is obtained by calculating the arithmetic mean of the absolute values of the surface deviation from the mean plane, divided by the measuring length.

Table 1 presents a summary of the different particle shapes, as well as other physical indicators, for all materials [24]. The determination of the maximum and minimum void ratios (e_{min} and e_{max}) of the test materials was conducted in accordance with the Chinese code GB/T 50123-2019 [52]. It is evident from Table 1 that frosted glass beads and round glass beads exhibit the highest level of sphericity and regularity, while convex glass beads and CDG sand possess extremely angular and irregular particle shapes. The particle shape of concave glass beads and Fujian sand, on the other hand, tends to be relatively spherical with a moderate level of angularity. Note that frosted glass beads and round glass beads are manufactured by different companies. Although both types are made from spherical glass, the sphericity, roundness, aspect ratio, and index void ratios [i.e., maximum and minimum void rations (e_{max} and e_{min})] of frosted glass beads are lower

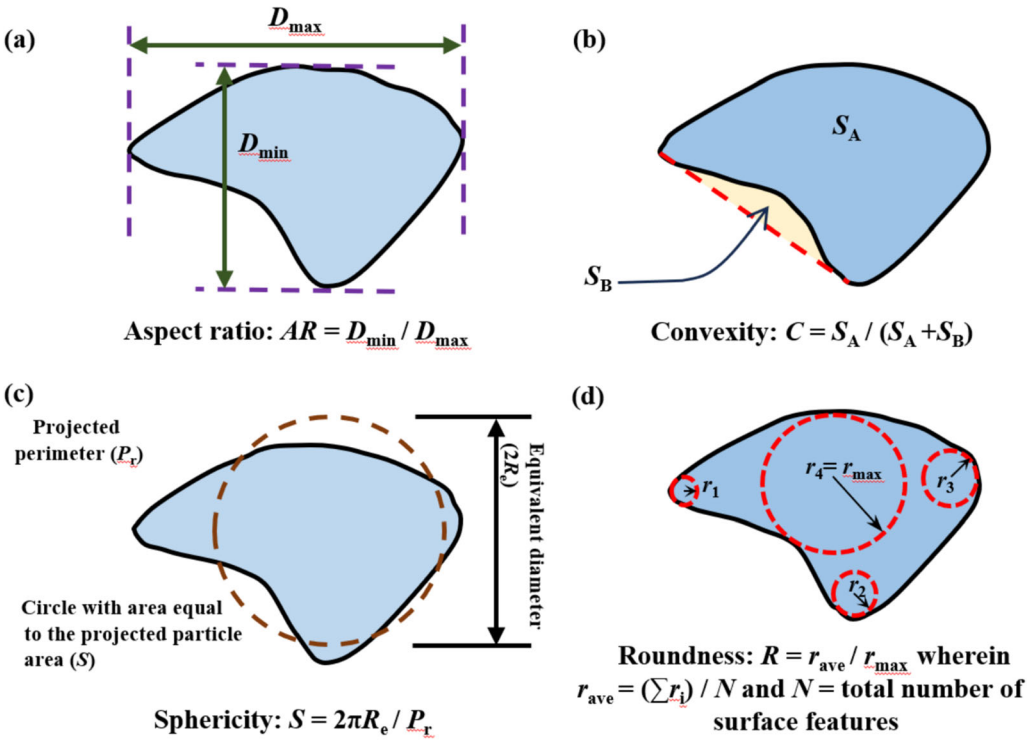

Fig. 2 Schematic for definitions of particle shape indices: **a** Aspect ratio; **b** Convexity; **c** Sphericity; **d** Roundness (Modified from Lashkari et al. [28])

compared to those of round glass beads. Additionally, angular materials, such as CDG sand and convex glass beads, display significantly larger index void ratios in comparison to rounded materials. However, mediumly angular materials, specifically concave glass beads, have the lowest index void ratios among all the materials. This suggests that the index void ratios do not follow a simple linear trend with the particle shape.

2.2 Test program

The shear wave velocity was measured using bender elements (BEs) that were installed in a triaxial apparatus manufactured by GDS Instruments Ltd. In Fig. 3, a pair of transmitter and receiver elements of BE were mounted in the top and bottom caps of the triaxial specimens. BE tests were conducted under triaxial boundary conditions, with shear waves propagating along the vertical height of specimens. By calculating the height of the specimen and the traveling time of the shear waves along the vertical axis of the specimen, the shear wave velocity (v_s) can be determined. Consequently, the maximum shear modulus can be calculated using the formula of $G_{max} = \rho v_s^2$, where ρ is the dry density. Prior to conducting tests with this system, the bender element underwent regular calibration and validation procedures, including delay time checks. The input signal utilized was a single-pulse sine wave with an amplitude of ± 14 V and excitation frequencies (f) of 10 kHz.

The triaxial specimen had a height of 100 mm and a diameter of 50 mm. The air pluviation method was utilized to prepare the triaxial specimens [22]. Each material was subjected to BE tests at three relative densities (D_r): D_r = 50%, 65%, and 80%. For coarse granular soils, it is widely accepted that the value of G_{max} in dry conditions is similar to that in water saturated conditions because water cannot sustain shear stress [9, 55]. In order to avoid the impact of pore fluid on shear wave propagation, dry specimens were used for small-strain dynamic tests, following general research methods [35, 37]. All samples underwent consolidation under isotropic conditions. As the suction inside the sample was gradually released, an initial confining stress of 30 kPa was applied. Subsequently, isotropic confining pressures were applied in steps as 50 kPa, 100 kPa, 200 kPa, 300 kPa, 400 kPa, 500 kPa, 600 kPa, 700 kPa, and 800 kPa. Axial strain during consolidation was calculated using displacement measurements. Note that the volumetric strain of the specimen was derived from the measured axial strain, following the experimental procedure of Liu et al. [37]. The measured void ratios of various materials are presented in Fig. 4, from which the dry density can also be derived.

Table 1 Physical properties of tested materials

Parameter	Round glass bead	Frosted glass bead	Concave glass bead	Convex glass bead	CDG sand	Fujian sand
Specific gravity	2.52	2.52	2.52	2.52	2.65	2.65
Maximum void ratio	0.780	0.761	0.640	1.142	1.346	0.884
Minimum void ratio	0.601	0.577	0.486	0.748	0.855	0.512
Mean grain size (mm)	1.5	1.5	1.5	1.5	1.5	1.5
Uniformity coefficient	1.455	1.455	1.455	1.455	1.455	1.455
Sphericity	0.954	0.954	0.903	0.888	0.854	0.896
Aspect ratio	0.971	0.960	0.712	0.697	0.686	0.720
Convexity	0.971	0.970	0.948	0.949	0.925	0.949
Roundness	0.958	0.951	0.689	0.553	0.543	0.625
Overall regularity	0.9635	0.95875	0.813	0.77175	0.752	0.7975
Average roughness (um)	1.445	1.921	1.626	1.680	1.975	1.423
A (MPa)	189.29	197.87	466.70	84.49	40.94	138.84
n	0.358	0.398	0.311	0.426	0.491	0.4
a	1.55	1.524	1.23	2.095	2.536	1.8

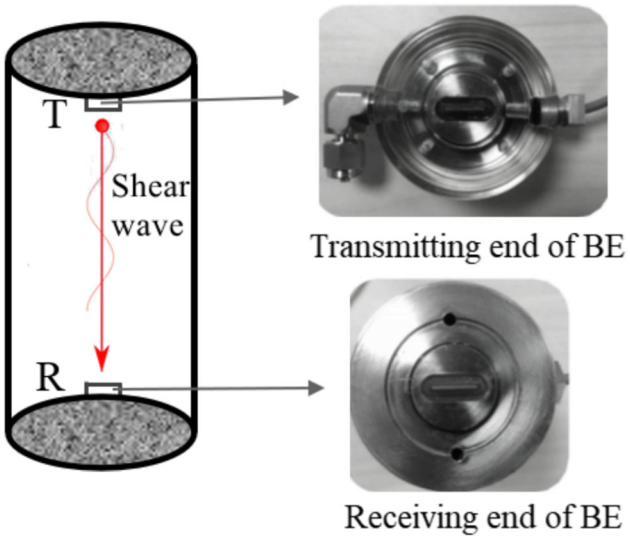

Fig. 3 Schematic for bender element

3 Test results and discussions

3.1 Effect of particle shape on G_{max}

Figure 5 depicts the typical waveforms of bender element tests, employing CDG sand as an example, at varying relative densities. Meanwhile, Fig. 6 compares the shear wave waveforms of different materials. The start-to-start method is commonly employed in BE tests for determining the shear wave velocity. The selection of characteristic points for the start-to-start method is based on the research conducted by Kawaguchi, et al. [26]. It can be observed that for the same material, the waveform remains similar under different relative densities, with the propagation time of shear waves increasing as the relative density decreases. However, under the same testing conditions, the waveforms of different materials exhibit significant variations.

Figure 7 shows the calculated G_{max} versus p' of all materials at different relative densities. To assess whether the near-field effect impacts the reliability of G_{max} results determined by the start-to-start method [4], the G_{max} values derived from shear wave velocity using the peak-to-peak method were included in Fig. 7 for comparison with those obtained from the start-to-start method. As p' increases and D_r decreases, G_{max} of granular materials gradually increases. Moreover, the G_{max} values derived from the peak-to-peak method and the start-to-start method demonstrate close agreement across the six granular materials, underscoring the high reliability of both approaches. Figure 8 compares the G_{max} values of different granular materials under the same D_r. As evident, regardless of the relative density, the G_{max} values can be ranked from small to large as follows: CDG sand, convex glass beads, round glass beads, frosted glass beads, Fujian sand and concave glass beads. This ranking roughly aligns with the order of void ratio from large to small at the same D_r. In comparison to rounded materials, angular materials exhibit higher void ratio, resulting in smaller G_{max} values. However, material with a medium angular shape (i.e., concave glass beads) displays the lowest void ratio and consequently the highest G_{max} values. These findings suggest that the influence of particle shape on G_{max} is predominantly determined by its impact on void ratio.

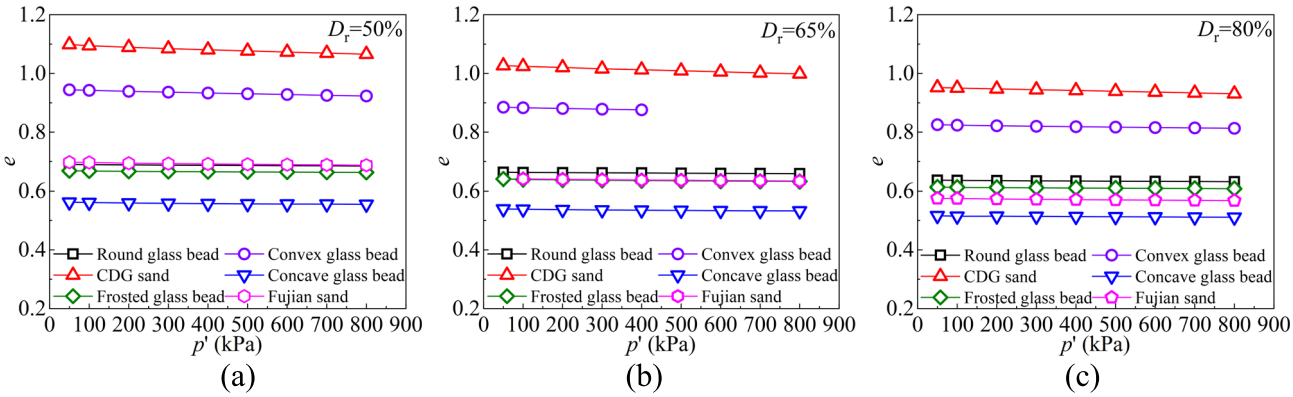

Fig. 4 Void ration after consolidation of all materials under: **a** D_r = 50%; **b** D_r = 65%; **c** D_r = 80%

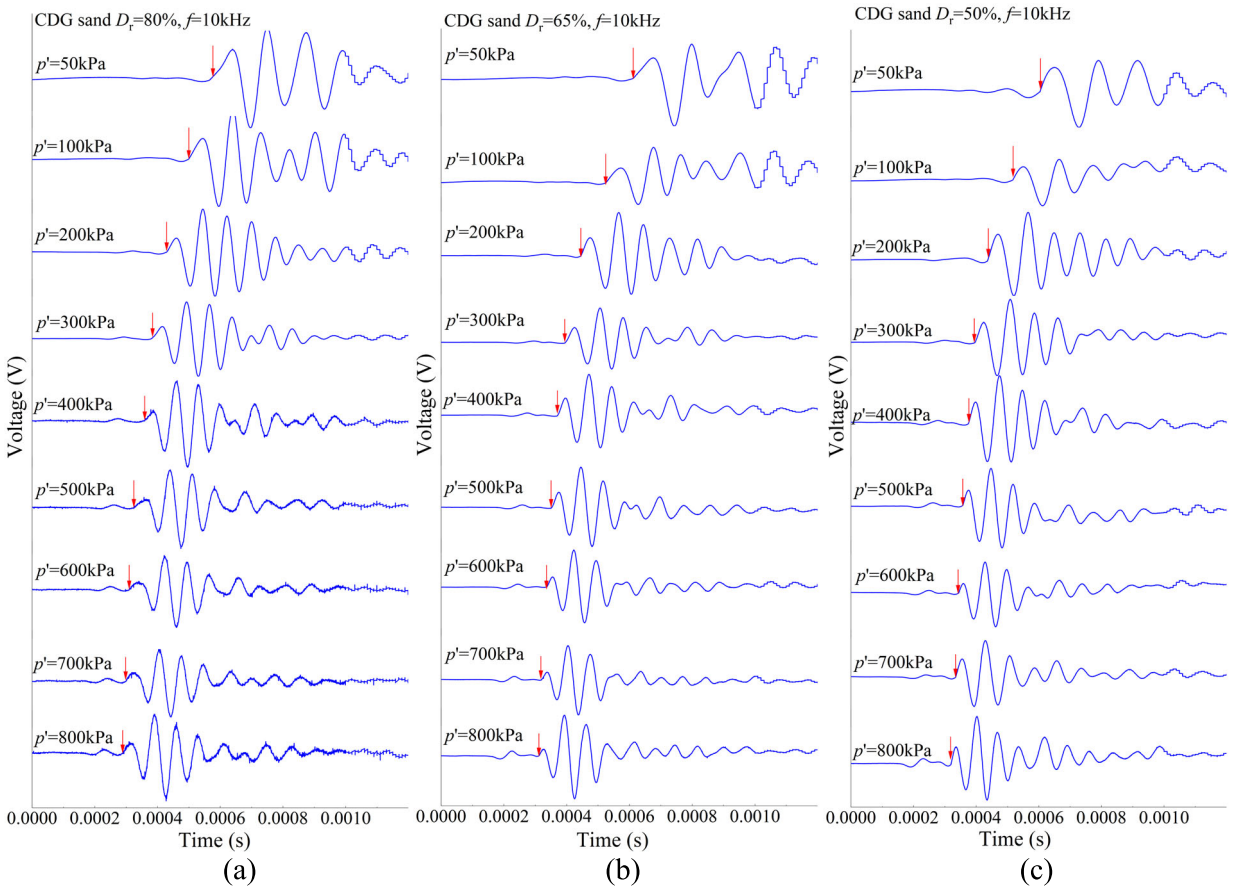

Fig. 5 Typical waveforms for CDG sand in BE tests under: **a** D_r = 80%; **b** D_r = 65%; **c** D_r = 50%

Figure 9 illustrates the relationship between G_{max} and particle morphology factors, using specific values of p' and D_r as examples. It is evident that as sphericity, aspect ratio, and roundness decrease, G_{max} initially increases and then decreases. This implies that within a certain range, an increase in the irregularity and angularity can contribute positively to the G_{max} characteristics of granular materials. The slight irregularity in particle shape is conducive to closer particle contacts and a reduced void ratio, which in turn fosters a more favorable fabric for the propagation of shear waves. However, if the irregularity of particle shape exceeds a certain threshold, a further decrease in sphericity and increase in angularity can result in a significant decrease in G_{max}. This demonstrates that when particle shapes become excessively irregular, the complex particle contacts lead to an unfavorable increase in the void ratio of

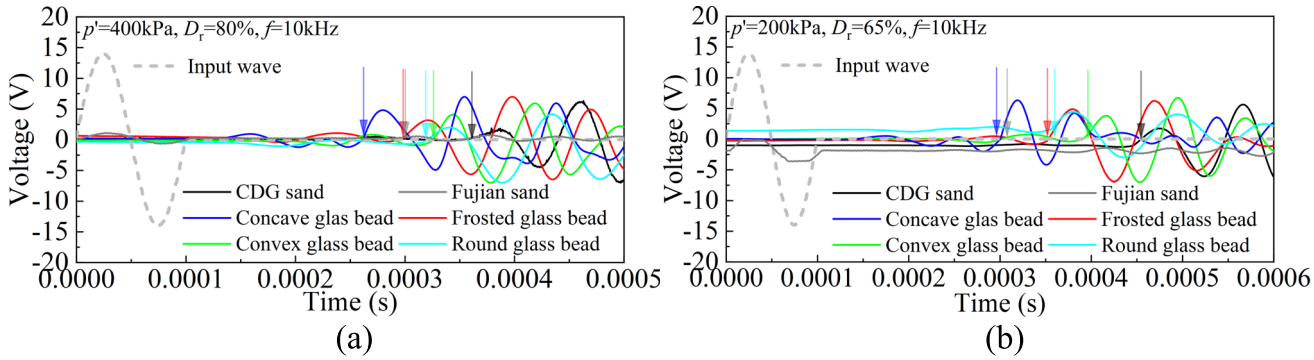

Fig. 6 Typical comparations of waveforms in BE tests for different materials under: **a** p' = 400kPa, D_r = 80%; **b** p' = 200kPa, D_r = 65%

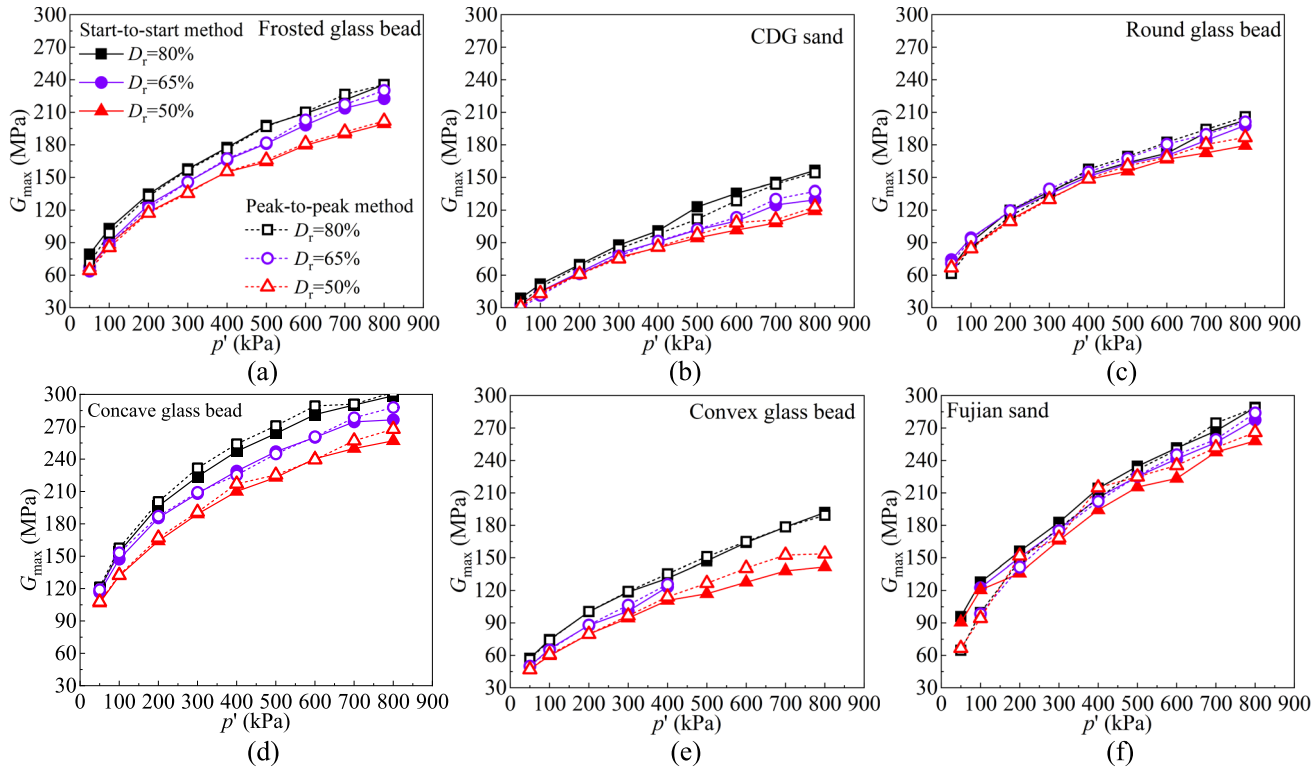

Fig. 7 Variations of G_{max} versus p' for: **a** Frosted glass beads; **b** CDG sand; **c** Round glass bead; **d** Concave glass bead; **e** Convex glass bead; **f** Fujian sand

the sample, thereby impeding the shear wave's transmission velocity. Whether rounded materials or angular materials have a larger G_{max} possibly depends on the degree of particle shape irregularity within a certain range. This evidence may shed light on the variability and difference in the superiority of G_{max} observed in previous studies involving rounded or angular materials.

3.2 Effect of particle shape on normalized G_{max}

The empirical relation proposed by Hardin and Black [16] is the most commonly used equation for estimating G_{max}, as shown below:

$$G_{max} = A\left(\frac{p'}{p_a}\right)^n F(e) \quad (1)$$

here, A is a material constant dependent on the soil type, p_a represents atmospheric pressure (100 kPa), n is an exponent, and $F(e)$ denotes the void ratio function. Previous studies have proposed various void ratio functions to describe the impact of void ratio (e) on G_{max} for granular materials. For instance, the Eq. (2) proposed by Hardin and Black [16] and Eq. (3) proposed by Oztoprak and Bolton [42] have been extensively utilized in existing research:

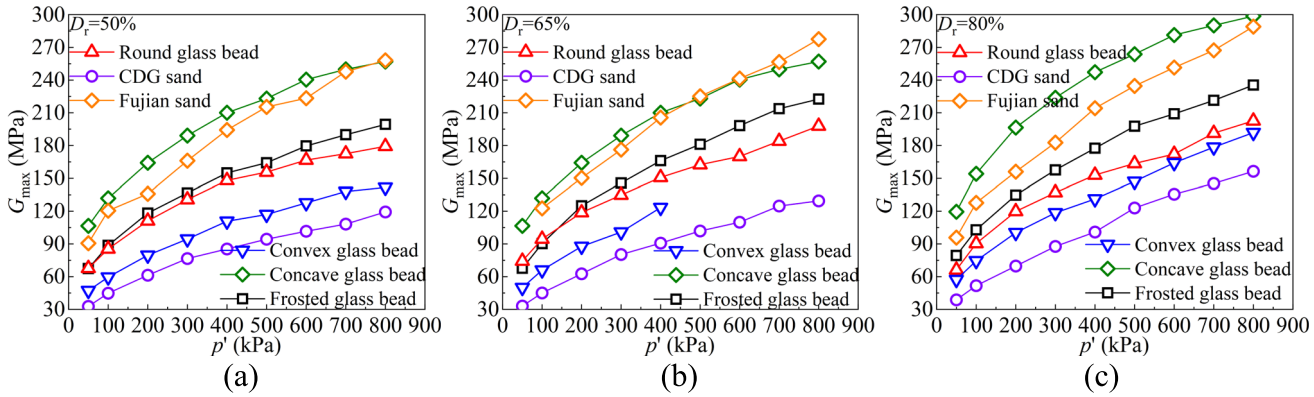

Fig. 8 Comparations of G_{max} of different materials under: **a** D_r = 50%; **b** D_r = 65%; **c** D_r = 80%

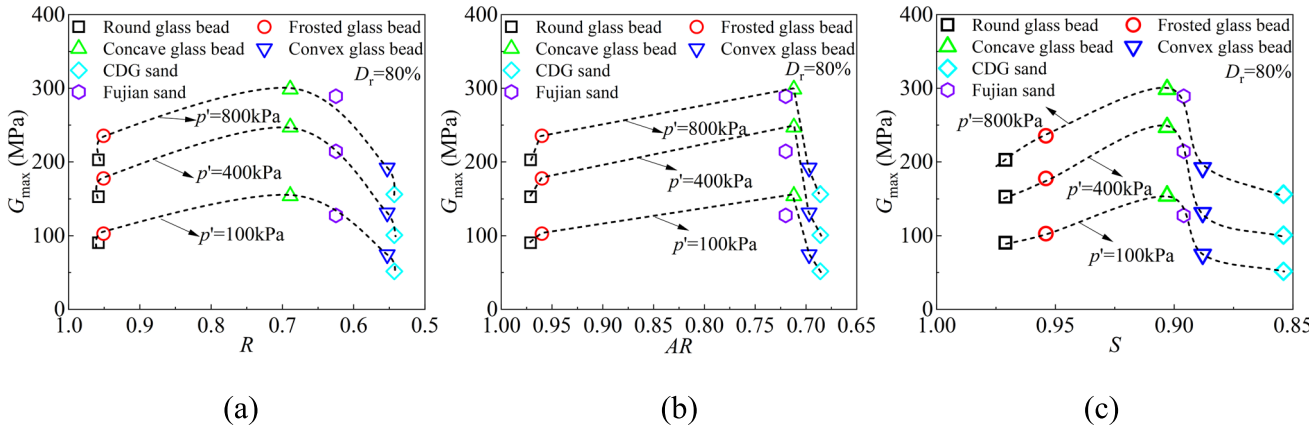

Fig. 9 Relationship between G_{max} with particle morphological factors

$$F(e) = \frac{(a-e)^2}{1+e} \tag{2}$$

$$F(e) = \frac{1}{(1+e)^3} \tag{3}$$

here, a is a material constant. Figure 10 displays the typical variations of G_{max} with void ratio (e), revealing that G_{max} of granular materials decreases as e increases. Both types of void ratio $F(e)$ functions were utilized to describe the effect of e on G_{max}, with fitting conducted using the function $G_{max} = kF(e)$. From Fig. 10, it can be observed that both functions effectively capture the e-induced effect, although Eq. (2) exhibits slightly higher accuracy. To achieve a fair and convenient comparison of normalized G_{max}, without being affected by the void ratio, Eq. (3) is employed to normalize G_{max}. Figure 11 shows the variation of normalized $G_{max}/F(e)$ with p' at different void ratios. Under a low mean effective stress, $G_{max}/F(e)$ of angular materials (i.e., CDG sand and convex glass bead) is significantly smaller than that of rounded materials and moderately angular material (i.e., concave glass bead). However, $G_{max}/F(e)$ of angular materials increases more rapidly with the increase of p'. This indicates that the G_{max} of materials with extremely angular shape is more sensitive to p'. Similar experimental results have also been reported by Cho, et al. [8] and Asadi, et al. [5].

3.3 Effect of particle shape on the parameters of the G_{max} prediction model

Regression analysis was performed on the G_{max} data for all materials using Eqs. (1–2), yielding the best-fitting parameters A and n, as presented in Table 1. By applying Eqs. (1–2) and the parameters A and n shown in Table 1, the G_{max} values for various materials can be accurately reproduced, as shown in Fig. 12. Figure 13 presents the variation of parameters A and n versus particle shape indicators. As observed from Fig. 13d–f, the exponent n exhibits an initial decrease, followed by an increase, as the sphericity (S), aspect ratio (AR), and roundness (R) of particles decreases. This implies that the sensitivity of G_{max} to p' in granular materials declines initially and then intensifies as the particles become more irregular and less spherical.

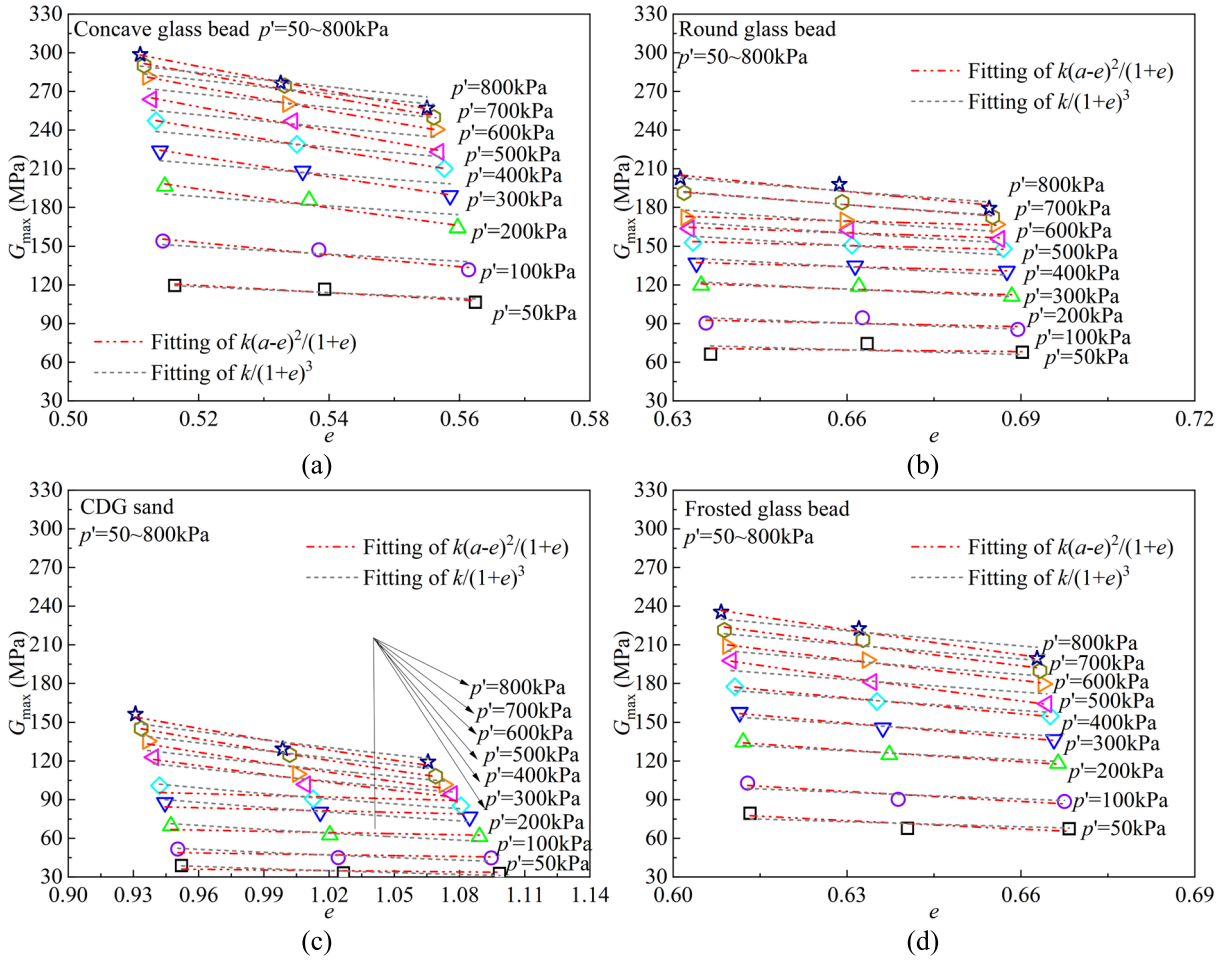

Fig. 10 Variations of G_{max} versus e for: **a** Concave glass beads; **b** Round glass beads; **c** CDG sand; **d** Frosted glass beads

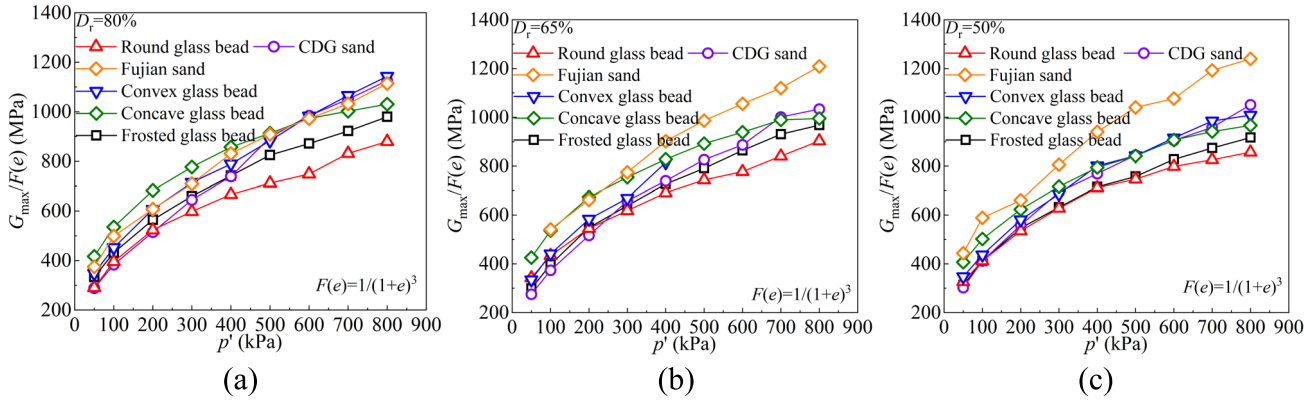

Fig. 11 Comparations of G_{max}/**Fe** versus p' for different materials under: **a** D_r = 80%; **b** D_r = 65%; **c** D_r = 50%

Parameter A represents the G_{max} value of granular materials under low confining pressures, specifically at the point when $F(e) = 1$ and $p' = p_a$. Figure 13a–c reveal that parameter A initially increases and then decreases with the decreases in sphericity, aspect ratio, and roundness. For materials with rounded shapes, particularly those with moderate angularity, such as concave glass beads, demonstrate higher G_{max} under low confining pressures, whereas angular materials exhibit extremely lower G_{max}. The relationship between $G_{max}/(p'/p_a)^n$ and e, obtained by normalizing G_{max} relative to the mean effective stress, is displayed in Fig. 14. It can be observed that materials with

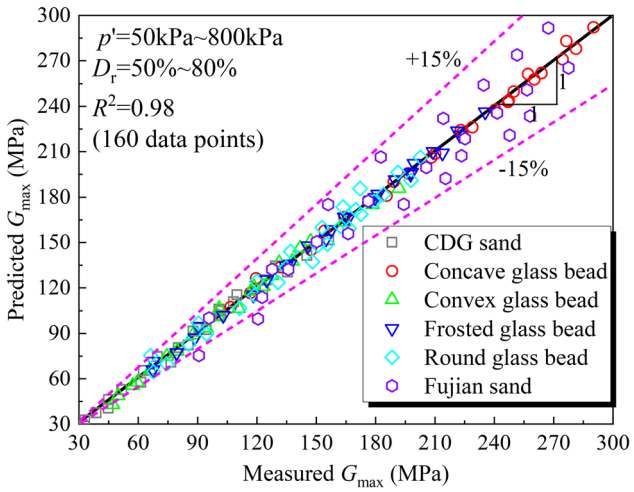

Fig. 12 Comparation of predicted G_{max} and measured G_{max} of all tests

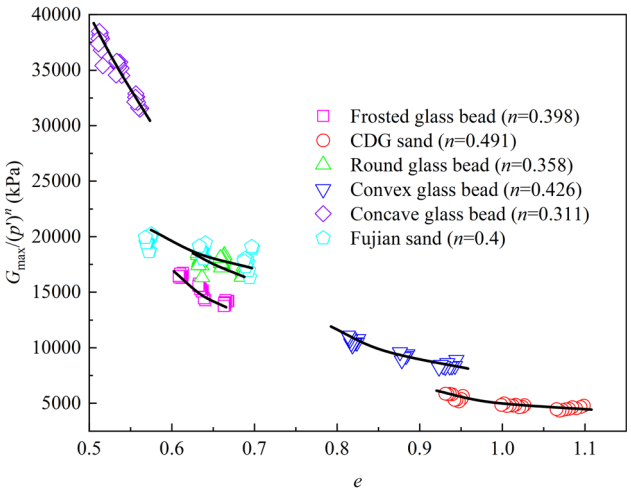

Fig. 14 $G_{max}/(p')^n$ versus e

moderate angularity, like concave glass beads, experience a substantial decrease in G_{max} as the void ratio increases. The decrease in G_{max} for rounded materials remains relatively gradual as the void ratio decreases. In contrast, the reduction in G_{max} for angular materials is much more gradual compared to other materials.

Numerous previous studies have highlighted the significance of developing the model to estimate the G_{max} of granular materials, as well as determining the G_{max} model parameters using various particle characteristics for practical engineering purposes [50, 51]. However, there is currently a controversy regarding the correlations between the parameters of the G_{max} prediction model and the particle morphology factors in existing studies. Specifically, while some studies have indicated that the parameter n, which quantifies the sensitivity of G_{max} to stress levels, tends to increase with greater particle shape irregularity

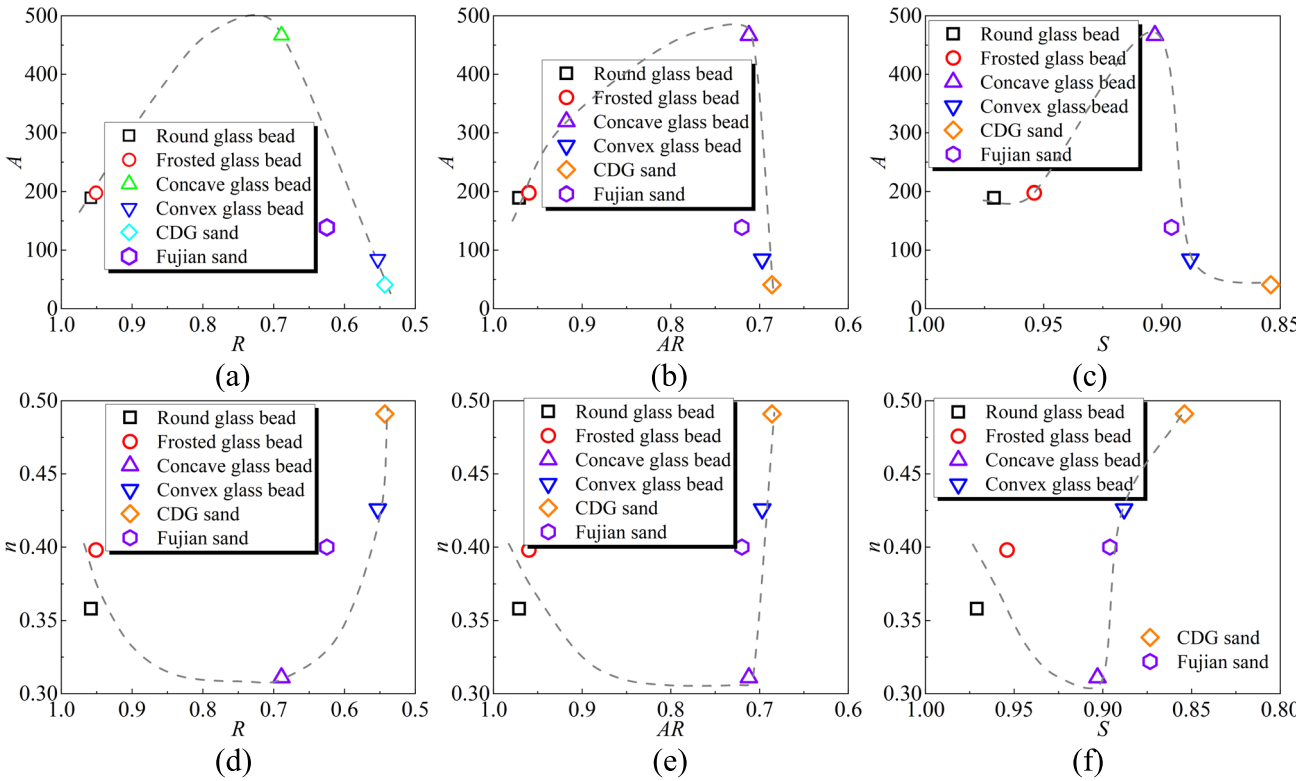

Fig. 13 Relationship between parameters A and n with particle morphological factors

[5, 8, 11], others have reported a contrasting trend, suggesting a decrease in n as particle shapes become more irregular [33, 34]. Through a comprehensive analysis of prior research and the data from this study, it has been revealed that the inconsistency in the G_{max} model parameters with respect to particle shape indices is likely associated with the range of the overall shape regularity. For example, Cho et al. [8] constructed a database encompassing the shear wave velocity of natural and crushed sands gathered from literature, and quantified the shape parameters for these sands. They observed that when roundness is larger than 0.8, an increase in roundness results in a decrease in the exponent β used to predict shear wave velocity (v_s) in the equation of $v_s = \alpha(p'/1\text{kPa})^{\beta}$, as shown in Fig. 15a. This suggests that as the particle shape becomes less spherical, the sensitivity of the shear modulus ($G_{max} = \rho v_s^2$) to p' reduces, i.e., parameters n reduces, consistent with findings reported by Asadi, et al. [5]. However, in the experimental results of Cho et al. [5], when roundness decreases to approximately 0.8, the trend of n decreasing with roundness diminishes. Additionally, in the research of Li, et al. [30], a considerable decreasing trend of β with respect to OR is observed when OR is smaller than 0.86 (see Fig. 15b). However, when OR is larger than 0.86, this decreasing rate gradually becomes slow and a further increase in OR only causes a slight increase in β. When particle shapes are relatively irregular, i.e., when OR falls within $OR \leq 0.825$, the decreasing trend observed in the literature is supported by the experimental data from this study. As shown in Fig. 16a, when OR is less than 0.825, the parameter n decreases significantly with increasing OR, indicating that the sensitivity of G_{max} to stress levels diminishes as particle shapes become more regular within this range. However, in Fig. 16a, when OR continues to increase beyond 0.825, a further rise in OR results in a slight increase in n. This rising trend in the higher OR range is supported by the experimental results of Liang, et al. [33], who fabricated granular materials with varying particle shapes using 3D printing and measured their shear moduli through bender element tests. They found that when OR exceeds 0.825, an increase in OR leads to a significant rise in n (see Fig. 15c), as reported by Liu and Yang [34]. Notably, in their study, 3D printing enabled the creation of perfectly spherical particles with $OR = 1$, whereas the spherical glass beads used in this study and in previous studies by Li et al. [29] only achieved an OR of approximately 0.96. This discrepancy may explain the more pronounced increase in n with OR in the higher OR range observed in the experiments of Liang et al. [33]. Based on the comprehensive analysis of experimental data from the literature and this study, it can be highlighted that the exponent n in Eq. (1) does not change monotonically with particle shape indicators but instead exhibits a turning point when particle shape indicators exceed a certain threshold. Consequently, the correlations between G_{max} prediction models and particle shape factors are established in Fig. 16 by compiling data on granular materials with diverse shapes from the literature and data gathered in this study.

Figure 16a summarizes the relationship between the parameters n and overall irregularity in this study and in previous literature. It can be noted that when the OR value is comparatively low, a decrease in OR leads to a reduction in the n-values. Nonetheless, when the overall irregularity (OR) exceeds 0.825, further reduction in OR results in an increase in n. The results in Fig. 16a illustrate that extremely irregular and spherical materials both exhibit higher sensitivity of G_{max} to p', while materials with moderately irregular particle shapes show the lowest sensitivity to p'. By conducting regression analysis, the transitional relationship between n and OR is delineated in distinct intervals as follows:

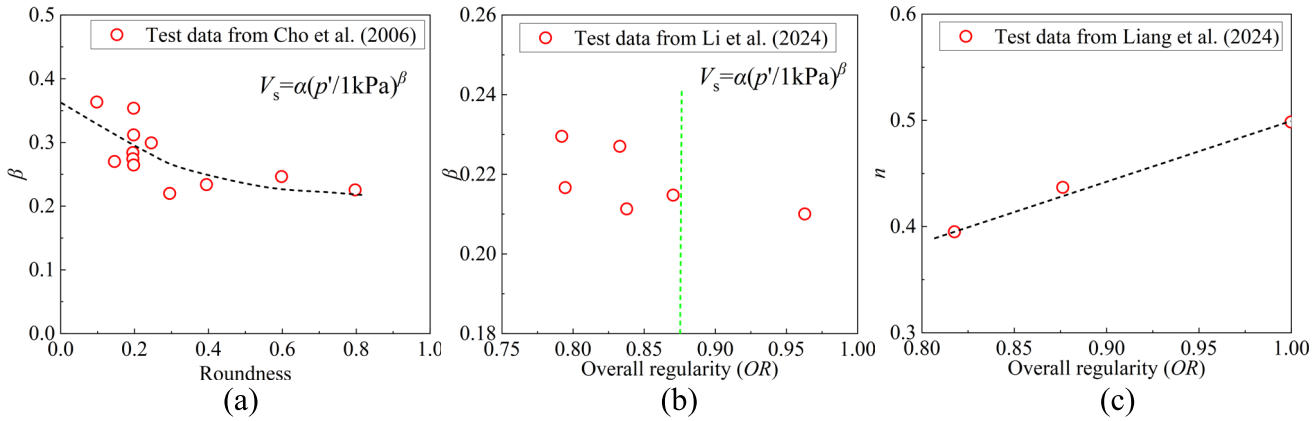

Fig. 15 Parameters β and n versus particle morphological factors in the literature: **a** β versus roundness; **b** β versus overall regularity; **c** n versus overall regularity

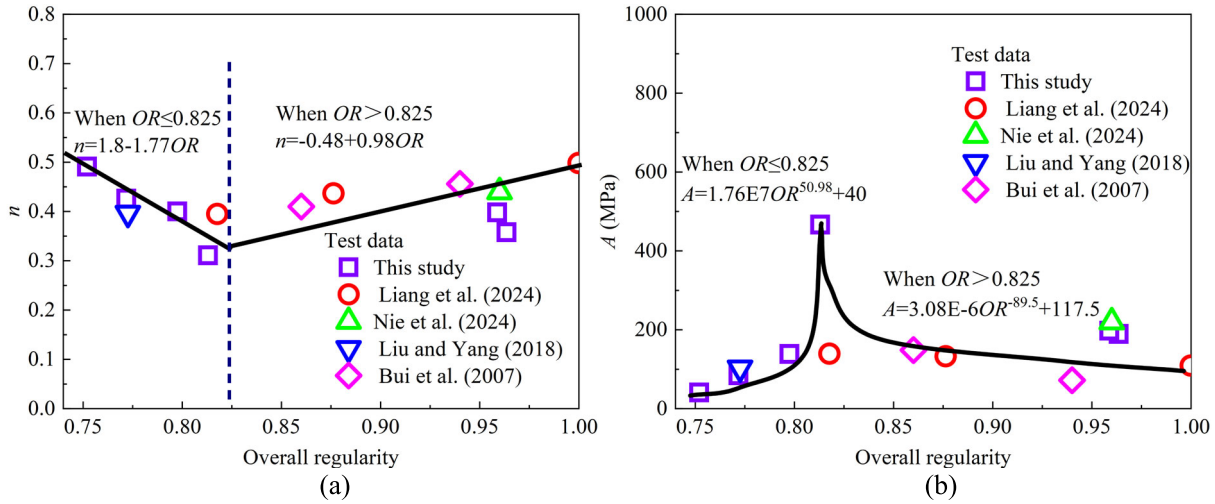

Fig. 16 Parameters n and A versus OR: **a** n; **b** A

$$\begin{cases} n = 1.8 - 1.77OR(OR \leq 0.825) \\ n = -0.48 + 0.98OR(OR > 0.825) \end{cases} \quad (4)$$

The influence of particle shape on n, i.e., the sensitivity of G_{max} to p', will be further elucidated using microstructural data obtained from CT scanning. Furthermore, Fig. 16b presents the transitional relationship between parameter A and overall regularity. Through systematically examining the test data in both this study and literature, an initial increase in parameter A followed by a subsequent decrease can be observed. The changes in parameter A can be expressed as a function of OR, as follows:

$$\begin{cases} A = 1.76\text{E}7OR^{50.98} + 40(OR \leq 0.825) \\ A = 3.08\text{E} - 6OR^{-89.5} + 117.5(OR > 0.825) \end{cases} \quad (5)$$

Equations (4–5) present the empirical relationships between n and OR, and A and OR, respectively, for the regression function $f(OR)$, aimed at isolating the influence of surface roughness. As depicted in Fig. 17a, $n/f(OR)$ generally shows a slight increasing trend with the average roughness index R_a, whereas $A/f(OR)$ displays more scattered variations with a less distinct decreasing trend with R_a. This suggests that a rougher surface texture tends to slightly reduce the shear modulus at 1 kPa under an equivalent e_0, while increasing the material's sensitivity to changes in stress levels. This observation is consistent with the findings of Li et al. [30] and Otsubo et al. [41], which emphasized the role of particle surface texture in models associated with the shear wave velocity of granular materials. Figure 17 isolates the effect of surface roughness from particle morphology, revealing that the relationships

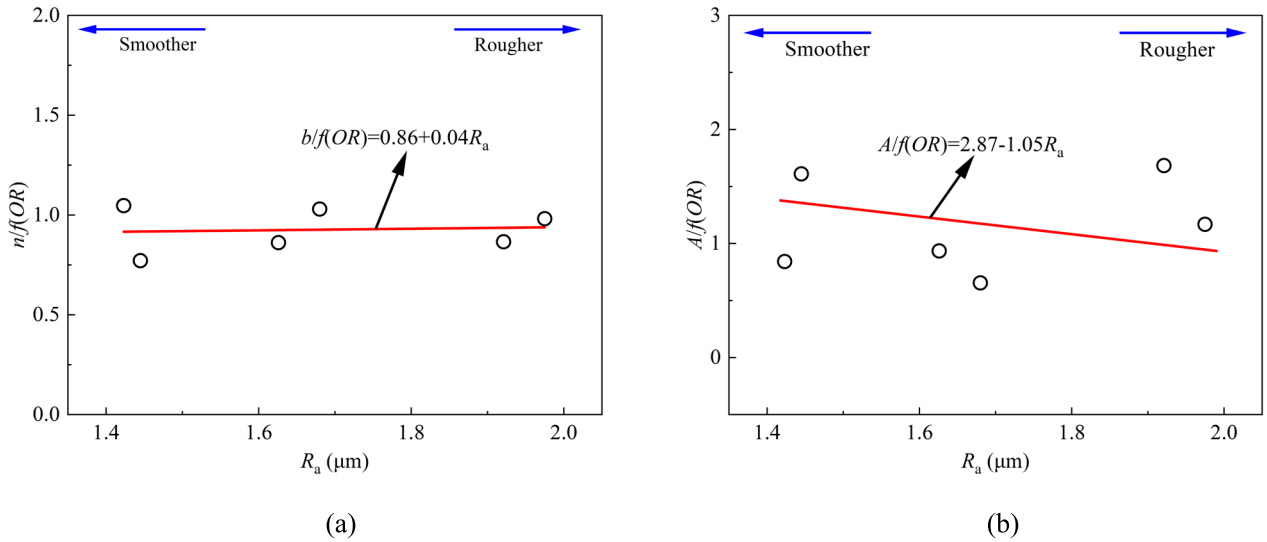

Fig. 17 Sensitivity of material constants (n and A) to surface roughness: **a** $n/f(OR)$; **b** $A/f(OR)$

between parameters A and n with surface roughness in the tested materials are relatively scattered. This further indicates that surface roughness exerts a less significant influence on the shear modulus compared to particle shape. This finding aligns with the results of Altuhafi et al. [3], who demonstrated that although particle shape plays a significant role in influencing various aspects of sand behavior, surface roughness does not appear to have a clear effect on any of the measured parameters, including stiffness.

4 Microstructure interpretation based on CT

4.1 CT tests

To provide a more thorough explanation regarding how particle shape affects shear wave velocity of granular materials from a microstructure aspect, computed tomography (CT) scans had been conducted by our group on dense granular material specimens (D_r = 80%) measuring 24.5 mm in diameter and 52 mm in height [21, 24]. These dimensions facilitate investigations into the contact mechanisms and initial fabrics of the specimens with different particle morphologies. In Figs. 18 and 19, representative parts of 2D cross-sectional images were selected and displayed for all materials to understand the microstructure. From Fig. 19b, d, it is evident that angular materials (e.g., convex glass bead and CDG sand) exhibit numerous large penetrating voids and thus loose particle contacts, compared to mediumly angular materials (e.g., concave glass bead) with the same relative density. Materials with higher angularity and elongated shape features display numerous surface-to-surface contacts (e.g., convex glass bead in Fig. 19b) and interlock structures (e.g., CDG sand in Fig. 19d). Moreover, as illustrated in Fig. 19c, the concave glass beads are tightly arranged even at initial state without confining pressure, with multiple particles in contact surrounding one individual particle (marked by a red dashed line).

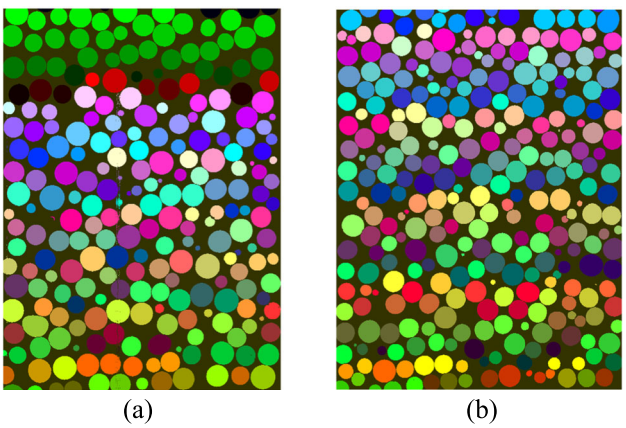

Fig. 18 Typical 2D cross-section of CT images for: **a** Round glass beads; **b** Frosted glass beads

4.2 LVMs-OT-based 3D particle reconstruction and imaging process

For deriving the microstructure parameters, such as particle contact orientation and coordination number. The innovative three-step methodology introduced by Li et al. [32], which leverages the capabilities of large vision models (LVM), has been employed to reconstruct three-dimensional (3D) individual particles from X-ray micro-computed tomography (μCT) images, as illustrated in Fig. 20. First, raw orthogonal images captured along the x-, y-, and z-axes are converted into two-dimensional (2D) segmentations by the LVM, which effectively identifies and labels the particles. Detailly, for a given slice along the z-axis, this slice is downsampled into a high-dimensional embedding via the image encoder of the LVM. Concurrently, a regular grid of point prompts is utilized to guide the LVM in pinpointing regions of interest within the image, thereby facilitating the identification of particles. For each prompt, the mask decoder assigns a confidence score that reflects the likelihood of the region being a particle. Regions with low confidence scores are filtered out, while those with high scores are retained, forming the initial 2D segmentation. To eliminate noises, threshold segmentation [1] is applied to transform the initial 2D segmentation into a more refined version.

Secondly, 2D segmentations along the x-, y-, and z-axes are converted to 3D segmentations using the optimal transport (OT) method. This method is applied between consecutive 2D segmentations to generate a relabeling scheme. For instance, the relabeling scheme $\pi_{i,i+1}$ provides instructions on how to relabel particles in the $(i + 1)$th 2D segmentation along the x-axis, ensuring that the same particle is consistently labeled across both the ith and $(i + 1)$th 2D segmentations. Finally, the 3D segmentations along the x-, y-, and z-axes are integrated to create a unified 3D segmentation where each particle is assigned a unique label, determined by the distinctiveness of voxels across the three 3D segmentations. Further details on the imaging process are available in Li et al. [32].

The coordination number Z, denoting the number of contacts per particle, is calculated by identifying inter-particle contacts. Contact detection is performed by dilating the 3D labels and analyzing pixel connectivity to determine particle pairs that share a common interface [27]. The mean coordination number $\overline{Z}$ within an assembly is defined as follows:

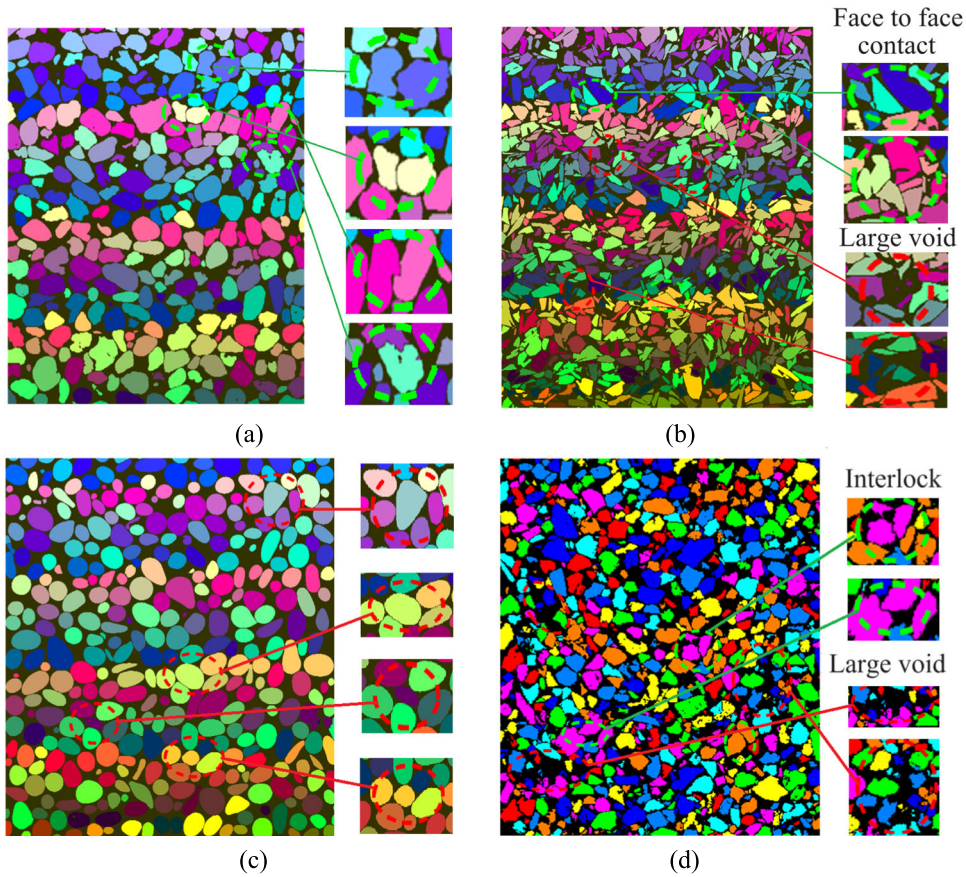

Fig. 19 Typical 2D cross-section of CT images for: **a** Fujian sand; **b** Convex glass beads; **c** Concave glass beads; **d** CDG sand

$$\overline{Z} = \frac{2N_c}{N_p} \tag{6}$$

where N_c and N_p denote the number of contacts and particles within the assembly, respectively.

Contact fabric, i.e., contact orientation, describes the anisotropic nature of the contact network and its influence on stress transmission. The fabric tensor $\boldsymbol{F}_{ij}$ is commonly expressed as:

$$\boldsymbol{F}_{ij} = \frac{1}{N_c}\sum_{k=1}^{N_c} n_i^{(k)} n_j^{(k)} \tag{7}$$

where $n_i^{(k)}$ and $n_j^{(k)}$ are the components of the unit normal vector of the kth contact. The eigenvalues and eigenvectors of $\boldsymbol{F}_{ij}$ characterize the principal directions and magnitude of contact anisotropy.

4.3 Microstructure interpretation

The relationship between the number of particle contacts and particle volume, derived from μCT data, is illustrated in Fig. 21. Figure 22a depicts the relationship between the statistically calculated mean coordination number ($\overline{Z}$) from Fig. 21 and the overall regularity (*OR*) for each material. When *OR* is below 0.825, the coordination number of the granular material increases with rising *OR*. However, when *OR* exceeds 0.825, a further increase in *OR* results in a reduction in $\overline{Z}$. This indicates that both highly irregular and regular particle shapes lead to a looser particle fabric with fewer coordination numbers, while moderately irregular particle shapes promote greater particle contact numbers. Figure 22b, c demonstrates the relationship between the mean coordination number and the parameters in the $G_{\max}$ prediction model. In Fig. 22b, as $\overline{Z}$ increases, parameter n exhibits a monotonically decreasing trend, indicating a reduced sensitivity of the materials' $G_{\max}$ to the stress levels. This observed phenomenon can be attributed to the fact that particle materials with lower mean coordination numbers, when subjected to higher stress levels, tend to rearrange and form more particle contacts, which facilitates shear wave propagation. In contrast, materials with higher coordination numbers possess a more stable internal structure that is less influenced by stress levels. Additionally, as $\overline{Z}$ increases, parameter A exhibits an increasing trend, suggesting that a larger $\overline{Z}$ enhances the shear modulus at 1 kPa under an equivalent e_0. The initially larger

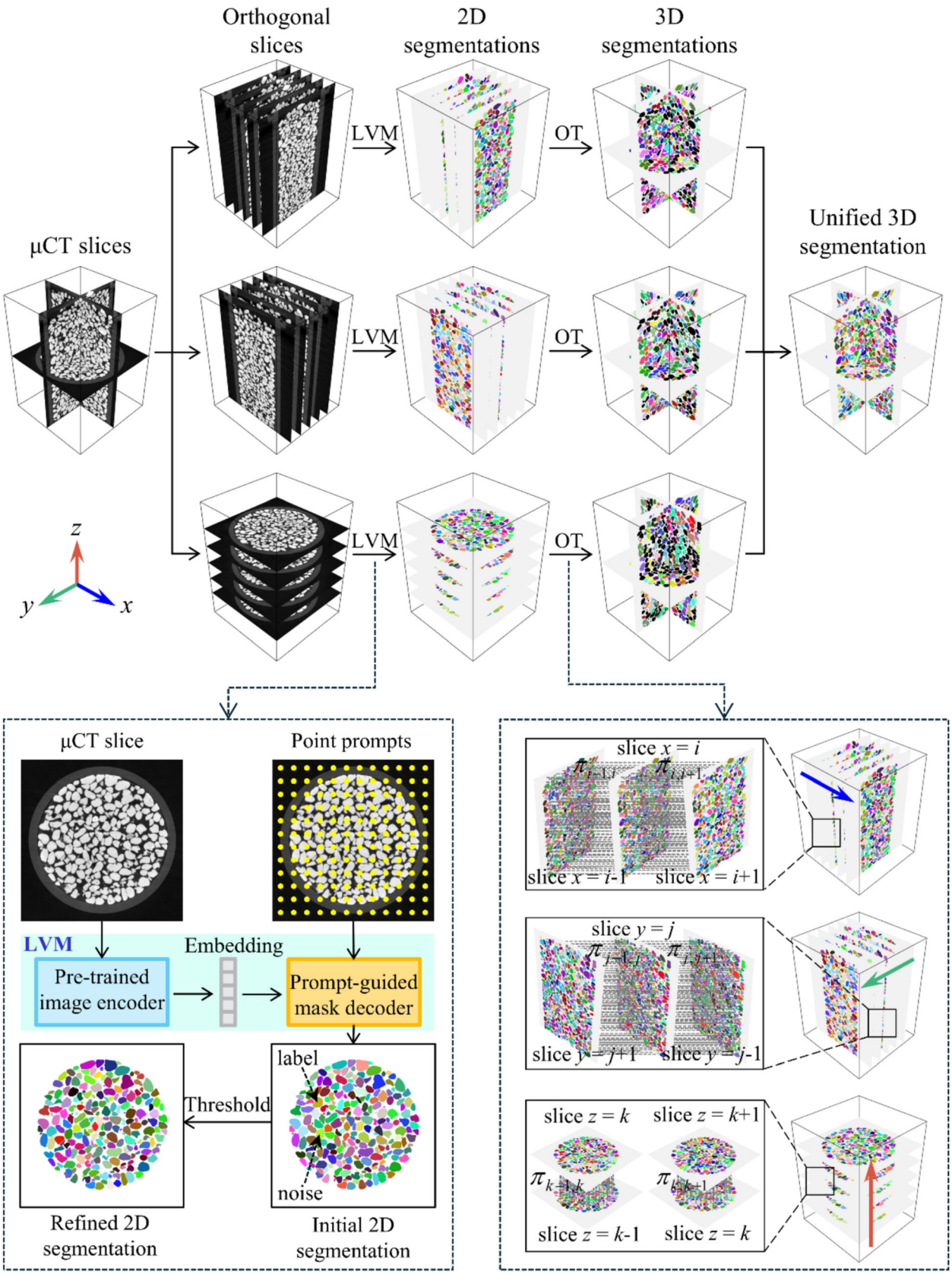

Fig. 20 Flowchart of particle reconstruction using LVM

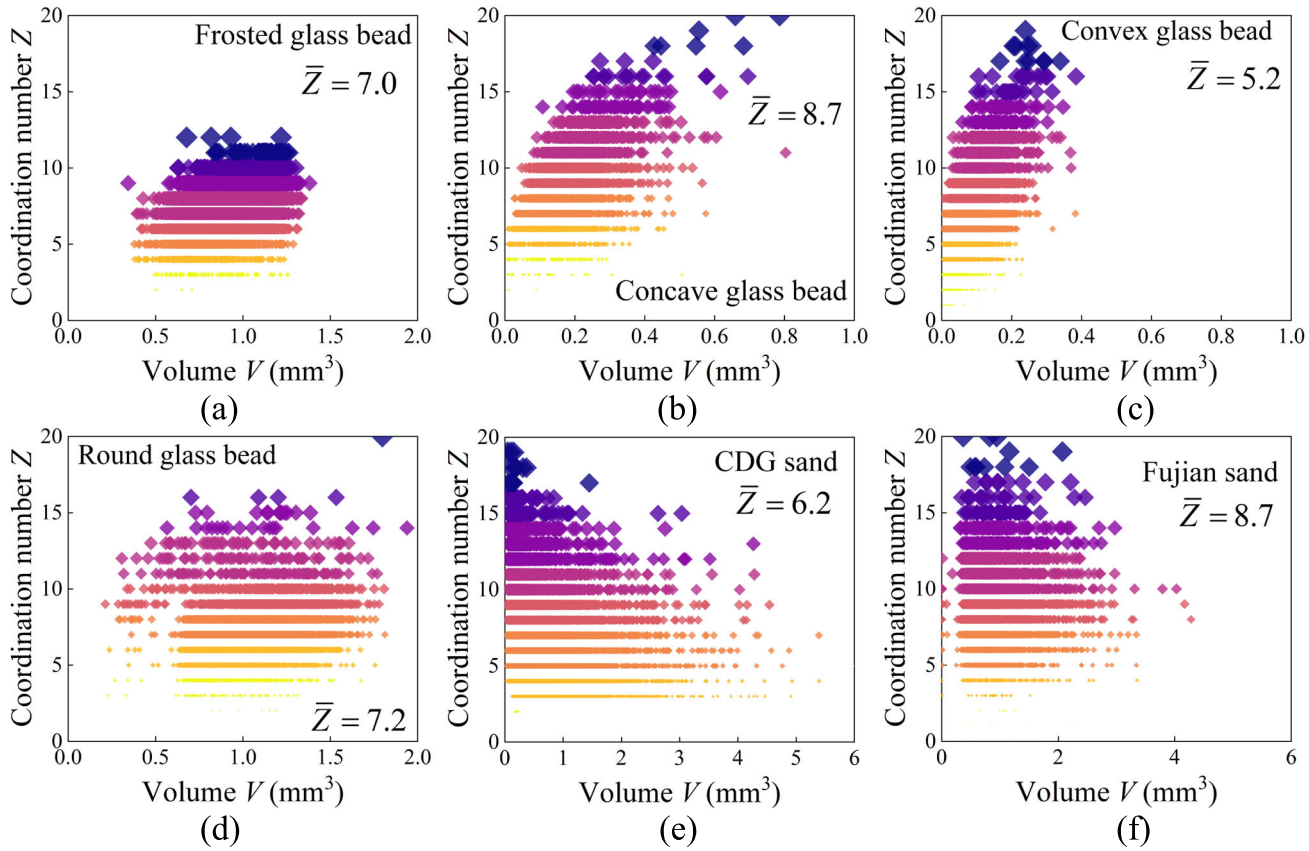

Fig. 21 Relationship between the number of particle contacts and particle volume for: **a** Frosted glass bead; **b** Concave glass bead; **c** Convex glass bead; **d** Round glass bead; **e** CDG sand; **f** Fujian sand

contact numbers of granular materials can contribute to a higher G_{max} at low p' values.

To investigate the contact fabric/orientation, Fig. 23 presents the contact normal distribution for the six materials. Due to gravitational effects during sample preparation, the long axis of the particles tends to align parallel to the horizontal/depositional plane, leading to a concentration of contact normal in the vertical direction. Furthermore, particle shape was found to influence the contact normal orientation of the materials. Compared to spherical glass beads with regular shapes, materials composed of irregularly shaped particles exhibit a more pronounced concentration of contact normal in the vertical direction. In contrast, spherical glass beads display a more isotropic distribution of contact orientations, with concentrations observed in multiple directions compared to irregularly shaped particles. In this study, the higher concentration of contact normal in the vertical direction may contribute to a greater shear modulus in the vertical direction than in the horizontal direction. However, the anisotropy of the shear modulus is not the primary focus of this study and warrants further exploration in future research.

5 Conclusions

To examine the impact of particle shape on the G_{max} of granular materials, six materials with a uniform size were chosen for comparison: two with a round shape, two with an angular shape, and two with a shape that was relatively spherical and mediumly angular. Particle shape measurement was carried out on these six materials. In addition, bender element tests were conducted under triaxial conditions on these granular materials at various mean effective stresses and relative densities. μCT scanning was carried out on cylindrical sand specimens to obtain microstructural fabric through image processing, which was utilized to explain the mechanism of G_{max}. The key findings of this study can be summarized as follows:

(a) Under the same relative density, as the irregularity of particle shape increased, the G_{max} of the materials first increased and then decreased. Angular materials had a lower G_{max} compared to rounded particles due to their larger void ratio. However, materials with a relatively spherical and moderately angular shape exhibited the lowest void ratio and, consequently, the highest G_{max} values. The influence of particle shape

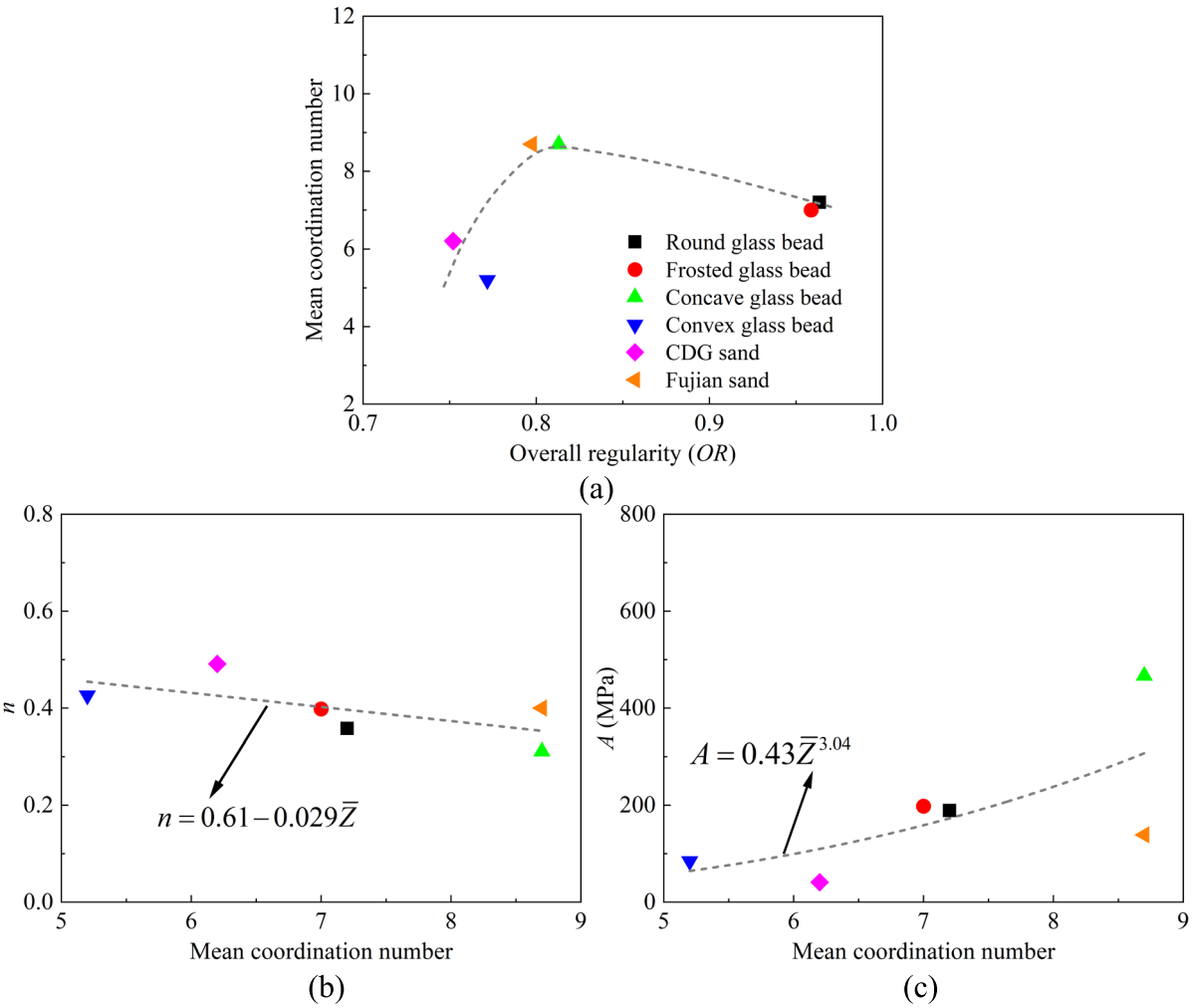

Fig. 22 Results of CT test: **a** Mean coordination number ($\overline{Z}$) versus overall regularity (OR); **b** n versus $\overline{Z}$; **c** A versus $\overline{Z}$

on G_{max} of granular materials depended significantly on its interaction with the void ratio.

(b) It was found that particle shape affected the sensitivity of G_{max} to the mean effective stress (p'). As particles became more irregular and less spherical, the sensitivity of G_{max} to p' initially decreased and then increased. This behavior could be attributed to the shape-dependent particle coordination number of sand specimens, as revealed by micro-CT test results. With an increase in overall regularity (OR), the mean coordination number ($\overline{Z}$) initially increased but declined once OR exceeded a certain threshold. As $\overline{Z}$ increased, the sensitivity of G_{max} to stress level, represented by the parameter n, monotonically decreased. This phenomenon might be explained by the fact that materials with lower coordination numbers, when subjected to higher stress levels, tended to undergo particle rearrangement and formed additional contacts, thereby enhancing shear wave propagation. In contrast, materials with higher coordination numbers exhibited a more stable internal structure that was less susceptible to changes in stress levels.

(c) Particle shape had a significant impact on the parameters of the G_{max} prediction model. Based on a careful synthesis and analysis of existing literature and experimental data from this study, it was highlighted that the parameters of the G_{max} prediction model did not monotonically change with the particle shape indicators, but instead showed a turning point when the particle shape indicators exceeded a certain threshold. As the overall regularity (OR) increased, the exponent n initially decreased and then increased, while the constant A first increased and then decreased. Equations for correlating the parameters of G_{max} prediction model with particle morphology were formulated and validated based on test data from granular materials with a

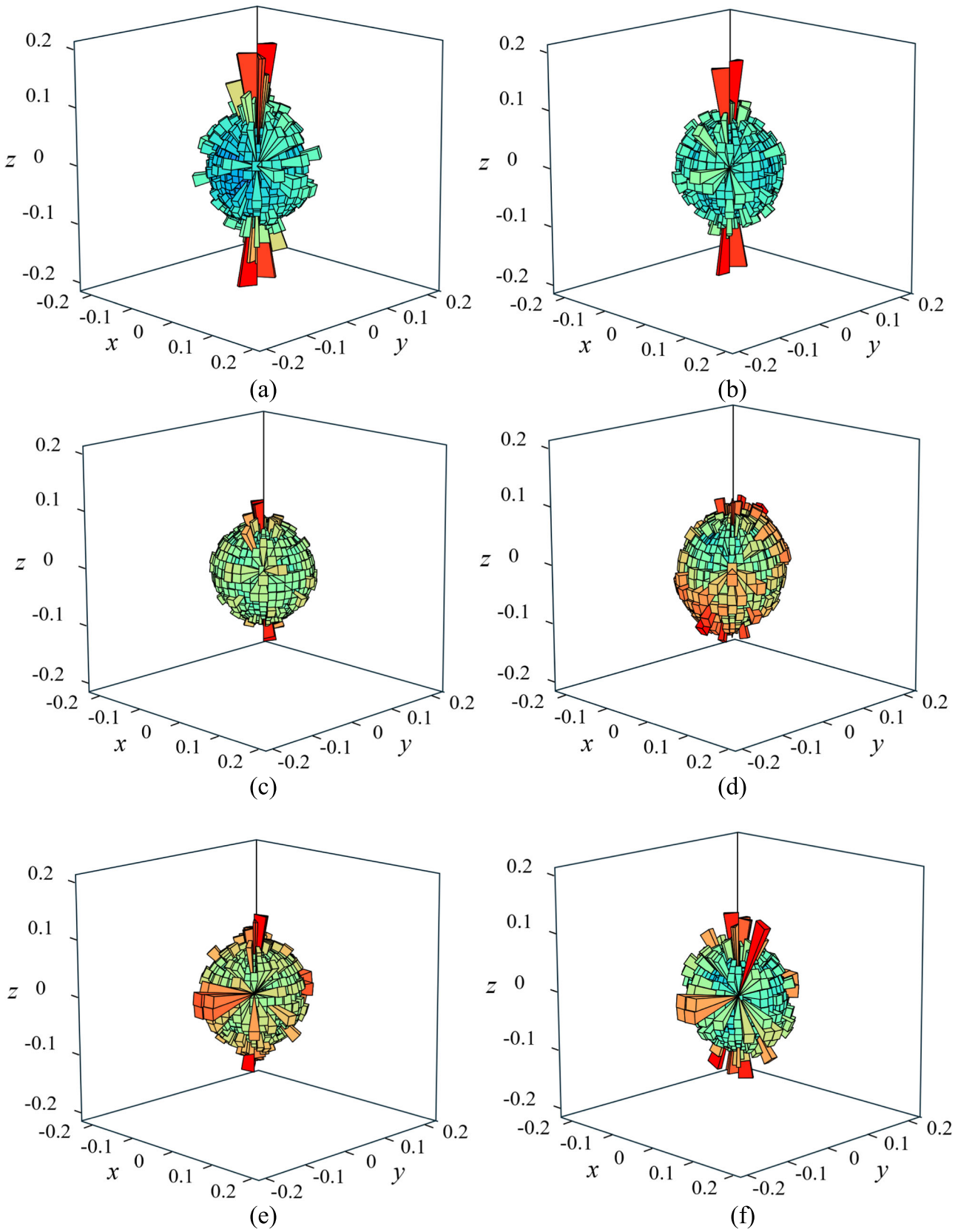

Fig. 23 Contact normal distribution for different materials: **a** Concave glass bead; **b** Fujian sand; **c** CDG sand; **d** Convex glass bead; **e** Frosted glass bead; **f** Round glass bead

wide range of particle shapes and transitional G_{max} response. Additionally, these formulas exhibited relatively weaker sensitivity to the surface roughness compared to the influence of particle shape.

Acknowledgements This research was financially supported by the Research Grants Council (RGC) of Hong Kong Special Administrative Region Government (HKSARG) of China (Grant no. 15220221, 15226822, 15227923, 15227624) and the National Natural Science Foundation of China (Grant no. 52178400).

Funding Open access funding provided by The Hong Kong Polytechnic University.

Data availability Data will be made available on reasonable request.

Declarations

Conflict of interest The authors declare that they have no competing financial interests or personal relationships that could have appeared to affect the work reported in this paper.

References

1. Al-Amri SS, Kalyankar NV (2010) Image segmentation by using threshold techniques. arXiv preprint arXiv:1005.4020
2. Alshibli KA, Alsaleh MI (2004) Characterizing surface roughness and shape of sands using digital microscopy. J Comput Civ Eng 18(1):36–45
3. Altuhafi FN, Coop MR, Georgiannou VN (2016) Effect of particle shape on the mechanical behavior of natural sands. J Geotech Geoenviron Eng 142(12):04016071
4. Arroyo M, Muir WD, Greening PD (2003) Source near-field effects and pulse tests in soil samples. Géotechnique 53(3):337–345
5. Asadi MB, Asadi MS, Orense RP, Pender MJ (2020) Small-strain stiffness of natural pumiceous sand. J Geotech Geoenviron 146(6):06020006
6. Bui MT, Clayton C, Priest JA (2007) Effects of particle shape on Gmax of geomaterials. In: Proc. 4th Int. conf. on earthquake geotechnical engineering
7. Cai Y, Dong Q, Wang J, Gu C, Xu C (2015) Measurement of small strain shear modulus of clean and natural sands in saturated condition using bender element test. Soil Dyn Earthq Eng 76:100–110
8. Cho G-C, Dodds J, Santamarina JC (2006) Particle shape effects on packing density, stiffness, and strength: natural and crushed sands. J Geotech Geoenviron 132(5):591–602
9. Clayton CRI (2011) Stiffness at small strain: research and practice. Géotechnique 61(1):5–37
10. Dutta TT, Otsubo M, Kuwano R, O'Sullivan C (2019) Stress wave velocity in soils: apparent grain-size effect and optimum input frequencies. Géotech Lett 9(4):340–347
11. Giang PHH, Van Impe PO, Van Impe WF, Menge P, Haegeman W (2017) Small-strain shear modulus of calcareous sand and its dependence on particle characteristics and gradation. Soil Dyn Earthq Eng 100:371–379
12. Goudarzy M, Rahemi N, Rahman MM, Schanz T (2017) Predicting the maximum shear modulus of sands containing non-plastic fines. J Geotech Geoenviron 143(9):06017013
13. Gu X, Yang J, Huang M (2013) Laboratory measurements of small strain properties of dry sands by bender element. Soil Found 53(5):735–745
14. Gu X, Yang J, Huang M, Gao G (2015) Bender element tests in dry and saturated sand: signal interpretation and result comparison. Soil Found 55(5):951–962
15. Hardin BO (1961) Study of elastic wave propagation and damping in granular materials. University of Florida
16. Hardin BO, Black WL (1966) Sand stiffness under various triaxial stresses. J Soil Mech Found Div 92(2):27–42
17. Hardin B, Drnevich V (1972) Shear modulus and damping in soil: measurement and parameter effects. Soils Mech Found Div 98:603–624
18. Hardin BO, Kalinski ME (2005) Estimating the shear modulus of gravelly soils. J Geotech Geoenviron 131(7):867–875
19. Hardin B, Richart FE (1964) Elastic wave velocities in granular soils. J Mech Found Div, Proc Am Soc Civil Engineers SM1 3407:33–65
20. He SH, Yin ZY, Ding Z (2025) Cyclic liquefaction of granular materials with varied forms under multidirectional loads. Géotechnique 75(2):243–257
21. He SH, Yin ZY, Ibraim E, Ding Z (2025) Face mask chips-reinforced sands under monotonic and cyclic torsional shearing. Géotechnique 1–16
22. He S-H, Ding Z, Xia T-D, Zhou W-H, Gan X-L, Chen Y-Z, Xia F (2020) Long-term behaviour and degradation of calcareous sand under cyclic loading. Eng Geol 276:105756
23. He S-H, Goudarzy M, Ding Z, Sun Y, Xu T, Zhang Q-F (2022) Small-strain shear modulus (Gmax) and microscopic pore structure of calcareous sand with different grain size distributions. Granul Matter 24(4):112
24. He SH, Yin ZY, Ding Z, Li RD (2025) Particle morphology and principal stress direction dependent strength anisotropy through torsional shear testing. Can Geotech J 62:1–23
25. JoviČIĆ V, Coop MR (1997) Stiffness of coarse-grained soils at small strains. Géotechnique 47(3):545–561
26. Kawaguchi T, Ogino T, Yamashita S, Kawajiri S (2016) Identification method for travel time based on the time domain technique in bender element tests on sandy and clayey soils. Soil Found 56(5):937–946
27. Kong D, Fonseca J (2019) On the kinematics of shelly carbonate sand using X-ray micro tomography. Eng Geol 261:105268
28. Lashkari A, Falsafizadeh SR, Shourijeh PT, Alipour MJ (2020) Instability of loose sand in constant volume direct simple shear tests in relation to particle shape. Acta Geotech 15(9):2507–2527
29. Li R, Gao X, He S-H, Ru D, Ding Z (2024) Fractal analysis of particle size and morphology in single-particle breakage based on 3D images. Fract Fract 8(11):614
30. Li Y, Otsubo M, Kuwano R (2024) Elastic wave velocities during triaxial shearing influenced by particle morphology. Soils Found 64(2):101443
31. Li Y, Otsubo M, Liu J, Kuwano R (2024) Effect of particle morphology on stress and strain characteristics of granular

materials during triaxial compression. Acta Geotech 19(5):2753–2773
32. Li R, Yin Z-Y, He S-H (2025) 3D reconstruction of arbitrary granular media utilizing vision foundation model. Appl Soft Comput 169:112599
33. Liang H, Shen Y, Chen S, Shen J, Xu J (2024) Effect of multi-scale particle morphology on small-strain shear modulus of irregularly shaped sand under isotropic consolidation: triaxial bender element tests on 3D-printed sand. J Eng Mech 150(4):06024001
34. Liu X, Yang J (2018) Shear wave velocity in sand: effect of grain shape. Géotechnique 68(8):742–748
35. Liu X, Yang J, Wang G, Chen L (2016) Small-strain shear modulus of volcanic granular soil: an experimental investigation. Soil Dyn Earthq Eng 86:15–24
36. Liu X, Zou D, Liu J, Zhou C, Zheng B (2020) Experimental study to evaluate the effect of particle size on the small strain shear modulus of coarse-grained soils. Measurement 163:107954
37. Liu X, Zou D, Liu J, Zheng B (2021) Predicting the small strain shear modulus of coarse-grained soils. Soil Dyn Earthq Eng 141:106468
38. Menq FY (2003) Dynamic properties of sandy and gravelly soils. Ph.D. thesis, University of Texas at Austin, Austin
39. Nie JY, Cui Y, Wang G, Wang R, Zhang N, Zhang L, Wu Z (2025) A comprehensive numerical investigation of multi-scale particle shape effects on small-strain stiffness of sands. Géotechnique 75(3):323–336
40. Otsubo M, O'Sullivan C (2018) Experimental and DEM assessment of the stress-dependency of surface roughness effects on shear modulus. Soils Found 58(3):602–614
41. Otsubo M, O'sullivan C, Sim WW, Ibraim E (2015) Quantitative assessment of the influence of surface roughness on soil stiffness. Géotechnique 65(8):694–700
42. Oztoprak S, Bolton MD (2013) Stiffness of sands through a laboratory test database. Géotechnique 63(1):54–70
43. Patel A, Bartake P, Singh D (2009) An empirical relationship for determining shear wave velocity in granular materials accounting for grain morphology. Geotech Test J 32:1–10
44. Payan M (2017) Study of small strain dynamic properties of sands and silty sands. UNSW Sydney
45. Rui S, Guo Z, Si T, Li Y (2020) Effect of particle shape on the liquefaction resistance of calcareous sands. Soil Dyn Earthq Eng 137:106302
46. Rui S, Guo Z, Si T, Zhou W, Zha X (2021) Particle shape influence on the deformation resistance of carbonate sands under drained condition. Soil Dyn Earthq Eng 144:106688
47. Salgado R, Bandini P, Karim A (2000) Shear strength and stiffness of silty sand. J Geotech Geoenviron 126(5):451–462
48. Sarkar D, Goudarzy M, Wichtmann T (2024) Influence of particle size on the small-strain stiffness in granular soils: experimental observations and micromechanical interpretation. Géotechnique 74(9):920–934
49. Sarkar D, Goudarzy M, Wichtmann T (2022) Inspection of various grain morphology parameters based on wave velocity measurements on three different granular materials. Soil Dyn Earthq Eng 153:107071
50. Senetakis K, Anastasiadis A, Pitilakis K (2012) The small-strain shear modulus and damping ratio of quartz and volcanic sands. Geotech Test J 35:1
51. Senetakis K, Madhusudhan BN (2015) Dynamics of potential fill–backfill material at very small strains. Soil Found 55(5):1196–1210
52. Standardization Administration of China M.o.C. (2019) China National Standards GB/T 50123–2019: standard for geotechnical testing method. China Planning Press, Beijing
53. Sun Y, Shen Y, Chen C (2017) A grading parameter for evaluating the grading-dependence of the shear stiffness of granular aggregates. Particuology 36:193
54. Wichtmann T, Triantafyllidis T (2009) Influence of the grain-size distribution curve of quartz sand on the small strain shear modulus Gmax. J Geotech Geoenviron 135(10):1404–1418
55. Yamashita S, Kawaguchi T, Nakata Y, Mikami T, Fujiwara T, Shibuya S (2009) Interpretation of international parallel test on the measurement of gmax using bender elements. Soil Found 49(4):631–650
56. Yang J, Gu XQ (2013) Shear stiffness of granular material at small strains: does it depend on grain size? Géotechnique 63(2):165–179
57. Youn J-U, Choo YW, Kim D-S (2008) Measurement of small-strain shear modulus Gmax of dry and saturated sands by bender element, resonant column, and torsional shear tests. Can Geotech J 45:1426–1438